

# Radio-Continuum Study of the Nearby Sculptor Group Galaxies. Part 3: NGC 7793 at $\lambda=12.2$ , 6 and 3 cm

Timothy J. Galvin, Miroslav D. Filipović, Nicholas F. H. Tothill, Evan J. Crawford, Andrew N. O'Brien • Nicholas Seymour • Thomas G. Pannuti, Alekzander R. Kosakowski, Biswas Sharma

**Abstract** We re-examine a series of archived centimetre radio-continuum observations ( $\lambda=16$ , 6 and 3 cm) focusing on NGC 7793 using the Australia Telescope Compact Array. These new images are both very sensitive ( $\sigma=0.011$  mJy/beam) and feature reasonably high angular resolution (down to  $<3''$ ). Using these images, a total of 76 discrete radio sources are identified, of which 57 have been classified. We also studied the radio component of the micro-quasar NGC7793-S26 which shows two distinct regions of somewhat steep spectral index ( $\alpha$ ) between  $-0.3$  and  $-0.7$ .

**Keywords** Galaxies: general Galaxies: NGC 7793 Radio continuum: galaxies

## 1 Introduction

As part of the Sculptor group galaxies, NGC 7793 is at an approximate distance of 3.91 Mpc (Karachentsev et al. 2003) and has been intimately examined throughout a number of multifrequency studies. Of particular interest is the source NGC7793-S26, initially discovered by Blair and Long (1997). Subsequent X-ray and Very Large Array (VLA) radio observations by Read and Pietsch (1999) and Pannuti et al. (2002) note extended emission associated with a bright

point source, designated S26. Further studies by Pakull and Grisé (2008), Pakull et al. (2010), Pannuti et al. (2011), and Dopita et al. (2012) examine this source in greater detail and suggest that it is micro-quasar in nature.

The Australia Telescope Compact Array (ATCA), having been upgraded with the Compact Array Broadband Backend (CABB) (Wilson et al. 2011), was used by Soria et al. (2010) to resolve S26's radio lobe structure and map its spectral index. As a part of our study of nearby Sculptor Group galaxies, we re-examine this data with an additional focus of discrete sources within NGC 7793's field.

Part 1 of this series of papers (Galvin et al. 2012) created a new set of highly sensitive and highly resolved mosaics of NGC 300 – another Sculptor Group galaxy – at  $\lambda = 20$  cm by combining ATCA and VLA data. Part 2, by O'Brien et al. (2013), re-examines ATCA and VLA data of the NGC 55 – yet another Sculptor Group galaxy – field at  $\lambda = 20$ , 13, 6 and 3 cm. In this paper we re-examine archived centimetre radio-continuum observations ( $\lambda=12.2$ , 6 and 3 cm) focusing on NGC 7793 using the ATCA with an additional focus on discrete sources. In §2 we describe the observational data and reduction techniques. We present and discuss our results in §3 and conclusion in §4.

---

Timothy J. Galvin, Miroslav D. Filipović, Nicholas F. H. Tothill, Evan J. Crawford, Andrew N. O'Brien

University of Western Sydney, Locked Bag 1797, Penrith, NSW, 2751, Australia

Nicholas Seymour

CSIRO Astronomy and Space Science, PO Box 76, Epping, NSW 1710, Australia

Thomas G. Pannuti, Alekzander R. Kosakowski, Biswas Sharma  
Space Science Center, Department of Earth and Space Sciences,  
Morehead State University, 235 Martindale Drive, Morehead, KY  
40351 USA

## 2 Data and data reduction

### 2.1 Observational Data

The data used in this study was obtained from the Australia Telescope Online Archive (ATOA)<sup>1</sup>. Project C2096 was conducted over 5 non-consecutive days using

---

<sup>1</sup><http://atoa.atnf.csiro.au/>

the ATCA and CABB, which provided a 2 GHz spectral window for each of the observations. The observations used in this study are summarised in Table 1.

In project C2096 we used PKS1934-638 and PKS2357-318 as its primary (flux and bandpass) and secondary (phase) calibrators, respectively. All observations used in this study were centred at RA (J2000)= $23^h57^m59.94^s$  and DEC (J2000)=- $32^\circ33'30.8''$ .

**Table 1** ATCA CABB C2096 observations used in this study. The bandwidth of all observations is 2 GHz.

Observation Date	Array	Central Frequency (GHz)	Time on source (hours)
6/08/2009	6D	5.5, 9	6.7
7/08/2009	6D	5.5, 9	6.2
27/06/2010	6C	5.5, 9	10.2
28/06/2010	6C	5.5, 9	9.8
29/06/2010	6C	2.45	9.9

## 2.2 Image Creation

The MIRIAD (Sault et al. 2011) and KARMA (Gooch 2011) software packages were used for data reduction and analysis. Typical MIRIAD calibration and flagging procedures were then carried out, including the use of the guided automatic flagging task PGFLAG.

Each observation was then imaged in order to verify its integrity. The task INVERT was used to produce a dirty map and beam. We found that supplying a Briggs robust parameter of 0.5 was the most effective in reducing the areas of sidelobe distortion. As we imaged the full spectral window provided by CABB, MF-CLEAN (Sault and Wieringa 1994) was used to deconvolve the multi-frequency synthesised dirty map. Finally, RESTOR and LINMOS were used to convolve and correct for primary beam attenuation.

Once we verified that sufficient data flagging and calibration had been carried out for each individual observation, a single image was created by combining datasets from all epochs for each particular frequency.

## 3 Results and Discussion

The final images produced in this study are presented in Figs. 1, 2 and 3. Each image was produced using the collective dataset for that particular frequency. We summarise the details and parameters of each image in Table 2.

Upon inspecting the final images we find that  $\lambda=12.2$  cm (Fig. 1) had a significantly higher RMS

noise level ( $1\sigma=0.30$  mJy/beam) than  $\lambda=6$  and 3 cm ( $1\sigma=0.011$  and  $0.015$  mJy/beam in Figs. 2 and 3 respectively). This was expected as NGC 7793 at  $\lambda=12.2$  cm was only observed for  $\sim 10$  hours, where as  $\lambda = 6/3$  cm was observed for  $\sim 33$  hours. As noise increased towards the edge of the primary beam, the adopted RMS values represent the upper limit in terms of local noise for each image. In the case of Fig. 3, approximately one third of the field of interest was ignored due to the increased confusion at the edge of the primary beam.

**Table 2** The image details of ATCA project C2096.

$\nu$ (GHz)	Beam Size (arcsec)	PA ( $^\circ$ )	RMS ( $\sigma$ ) (mJy/beam)	Figure #
2.4	$7.6\times 3.8$	2.4	0.030	1
5.5	$3.6\times 1.8$	1.0	0.011	2
9.0	$2.2\times 1.1$	-1.1	0.015	3

### 3.1 Discrete sources within the field of NGC7793

We initially searched for sources in each image using the automated MIRIAD task SFIND. Using the returned results as a starting point list, we then reviewed each listed source in the field to evaluate its reliability. A number of proposed sources from SFIND were discounted as they were either artefacts of side-lobes around particularly strong points or were outside the field of NGC 7793. After removing such sources, we then manually examined each image to identify any remaining sources which were not found by SFIND. The red ellipse in Figs. 1, 2, 3 and 4 highlights the field which was searched for sources and was constructed to tightly cover the centre of NGC 7793 as seen from the Digital Sky Survey <sup>2</sup> (DSS) optical image. The size of the major and minor axis of this ellipse is approximately  $7.78''$  by  $4.90''$  at a position angle of  $280^\circ$ .

A total of 76 discrete sources above  $3\sigma$  (0.090, 0.033 and 0.045 mJy/beam at wavelengths 12.2, 6 and 3 cm (Table 3; Column 5, 6 and 7 respectively) were identified within the field of NGC 7793. Using a  $5''$  search radius, a value adopt because of the beam size of Fig. 1, a total of 39 sources were found at more than one wavelength. In such cases we estimated sources spectral index,  $\alpha$ , defined as  $S \propto \nu^\alpha$  (Table 3; Column 12). When calculating this spectral index value we assumed a error in flux density of 10% for each measurement. Position, integrated flux densities and spectral indices of these catalogued sources are presented in Table 3. The positions listed in Table 3 refer to the location of each

<sup>2</sup>[http://archive.stsci.edu/cgi-bin/dss\\_form](http://archive.stsci.edu/cgi-bin/dss_form)

**Fig. 1** Project C2096 at  $\lambda=12.2$  cm in mJy/beam. The red ellipse highlights the area that was examined for sources. The beam is  $7.6'' \times 3.8''$ , as represented by the blue ellipse in the bottom left corner. The primary beam was blanked after  $23'$ .

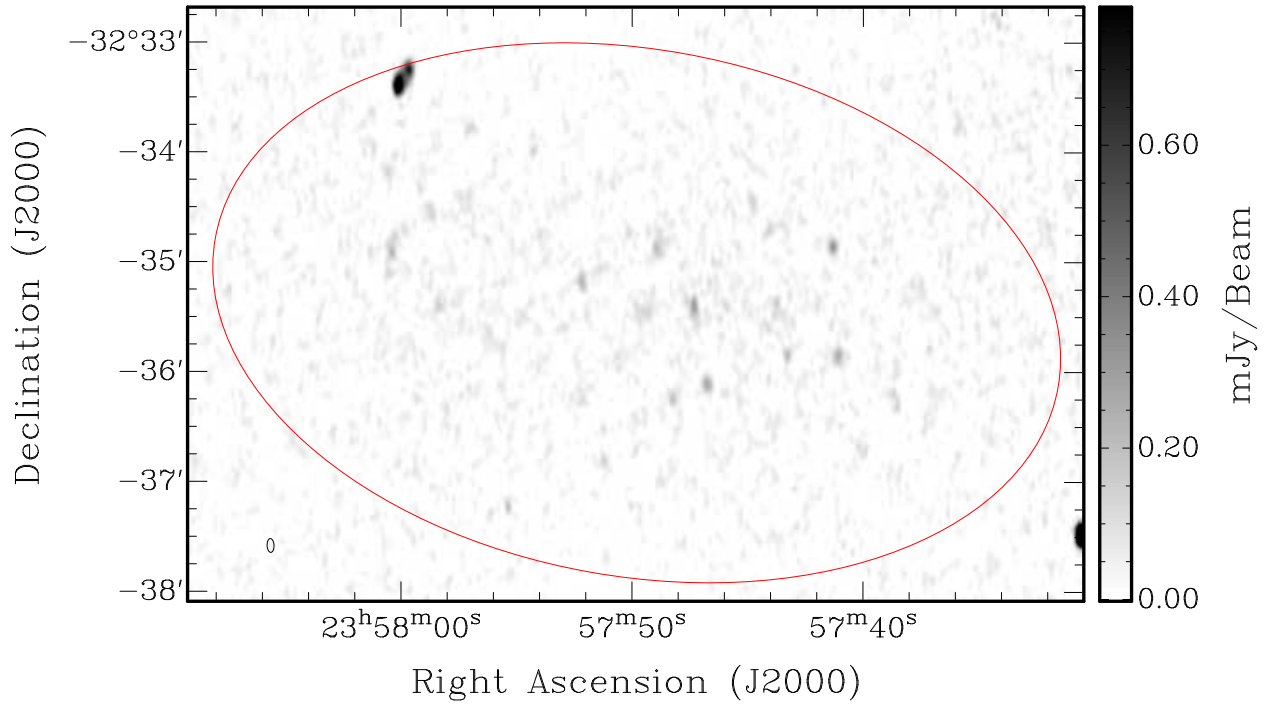


**Fig. 2** Project C2096 at  $\lambda=6$  cm in mJy/beam. The red ellipse highlights the area that was examined for sources. The beam is  $3.6'' \times 1.8''$ , as represented by the blue ellipse in the bottom left corner. The primary beam was blanked after  $9.08'$ .

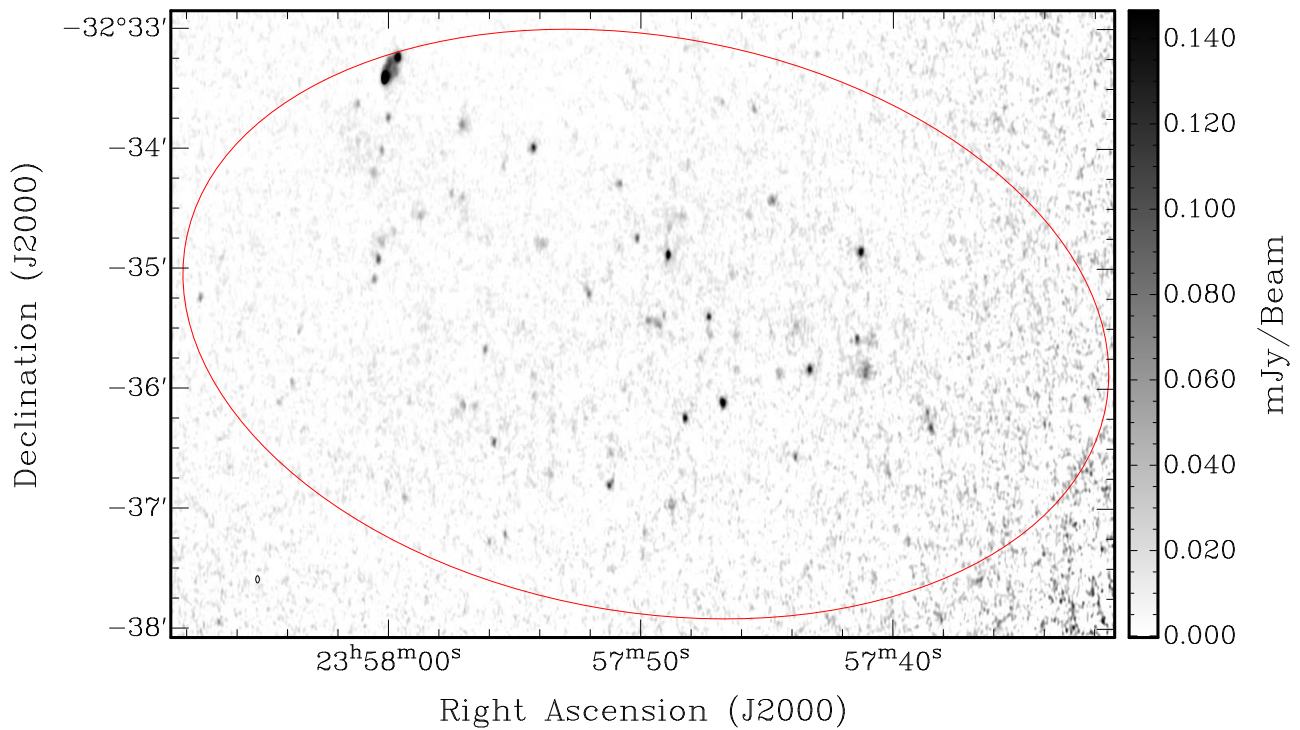
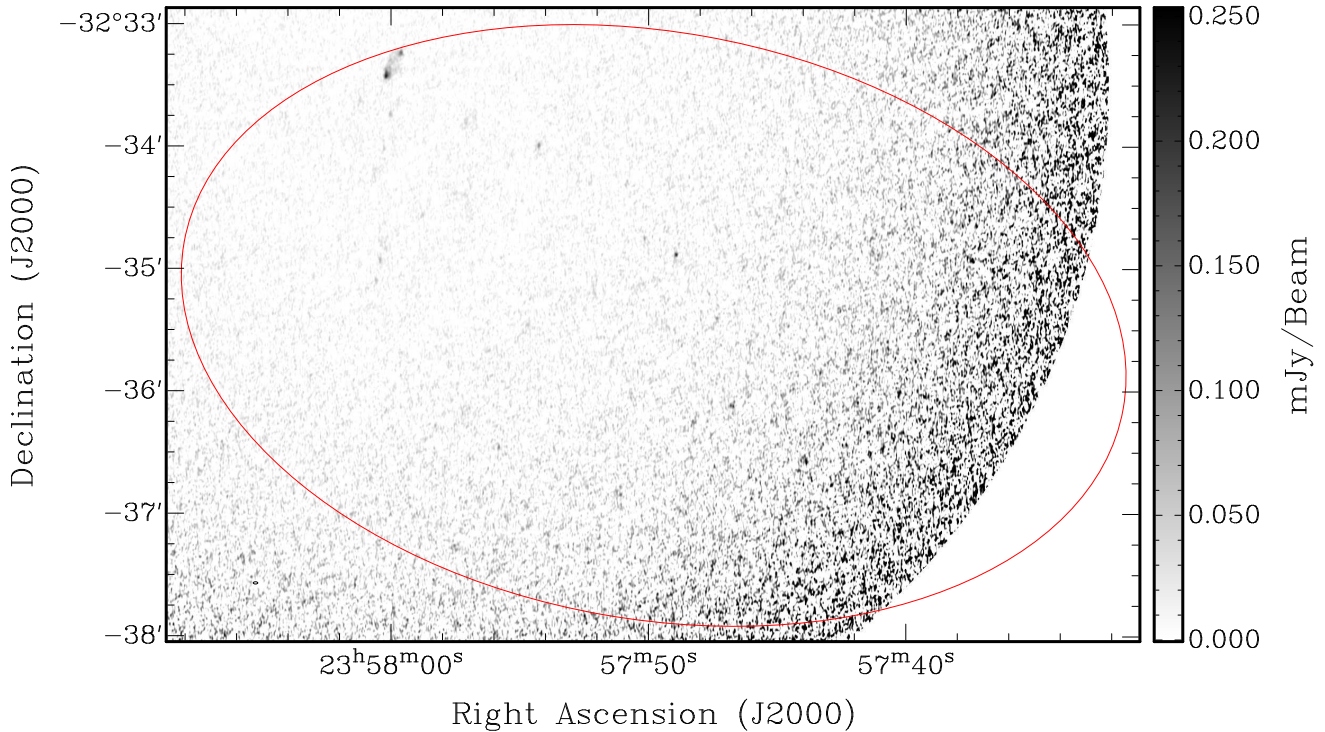


**Fig. 3** Project C2096 at  $\lambda=3$  cm in mJy/beam. The red ellipse highlights the area that was examined for sources. The beam is  $2.2'' \times 1.1''$ , as represented by the blue ellipse in the bottom left corner. The primary beam was blanked after  $5.86'$ .



source from the highest frequency image from which it was found. Due to the smaller primary beam at  $\lambda = 3$  cm (Fig. 3), approximately one third of the search ellipse is too noisy for source detection. The 28 sources within this flagged area have been marked in Table. 3 with †.

Our new catalogue of 76 discrete radio-continuum sources in NGC 7793 was then compared to the Infrared (Kennicutt et al. 2003), Ultra-violet (Dale et al. 2009), Optical (DSS) and X-ray (Pannuti et al. 2011) catalogues and any source coincidences that were found using a search radius of  $5''$  were noted in Table 3 (Columns 8, 9, 10 and 11 respectively).

In Fig. 5 we show the distribution of integrated flux densities of detected sources at  $\lambda = 12.2, 6$  and  $3$  cm as described in Table 3 (Columns 5, 6 and 7 (excluding NGC7793-S26 (Table. 3; Index 61))). We note that the majority of sources (85%) have an integrated flux density that is below  $10\sigma$  flux density levels. Fig. 6 shows the distribution (in terms of spectral index (Table. 3; Column 12) and classification (Table. 3; Column 13)) of 38 out of the 76 sources identified in this study. J235743–323634 (Table. 3; Index 13) is excluded from this graph. We note two distinctive source groups; one peaking at  $\alpha=-0.6$  and second at  $\alpha=-0.2$ . Out of 39 sources with an estimated spectral index, 24 (61.5%) can be classified as having a flat or inverted spectrum

with an  $\alpha$  between 0.7 and  $-0.5$ . The remaining 15 sources (38.5%) have a steeper  $\alpha$  between  $-0.5$  to  $-1.7$ .

### 3.2 Source Classification

Seventy-six (76) radio-continuum sources were detected in our study. These sources have been classified into three main groups: background sources, Supernova Remnants (SNRs) and HII regions. Combining previous work and our new radio-continuum maps we classify a total of 57 sources. From these 57 sources, 37 are most likely to be HII regions, 14 to be SNRs, 1 to be a micro-quasar (see Pakull and Grisé (2008), Pakull et al. (2010), Pannuti et al. (2011) and Dopita et al. (2012)), 1 to be a background galaxy (or AGN) and 4 which could be either an SNR or a background galaxy (or AGN). The remaining 19 radio-continuum sources still have no classification. We list each sources classification, where appropriate, in Table 3; Column 13. Strong candidates are listed as either HII, SNR, MQ (micro-quasar) or BCKG (background galaxy/AGN), while weaker candidates are listed as hii, snr and bckg. Fig. 6 shows the distribution of these source classifications.

A source was classified as a strong candidate SNR if it had both a steep negative spectral index and an X-Ray counterpart. If a source only had one of these

**Fig. 4** Spectral index pixel map of NGC 7793 as calculated from  $\lambda = 12.2, 6$  and  $3$  cm data. The image is in terms of spectral index  $\alpha$ , where  $\alpha$  is defined as  $S \propto \nu^\alpha$ . The red ellipse highlights the area that was examined for sources and the colour bar on the right reflects the spectral index value. The synthesised beam, represented by the blue ellipse in the lower left corner, is  $7.56'' \times 3.80''$ .

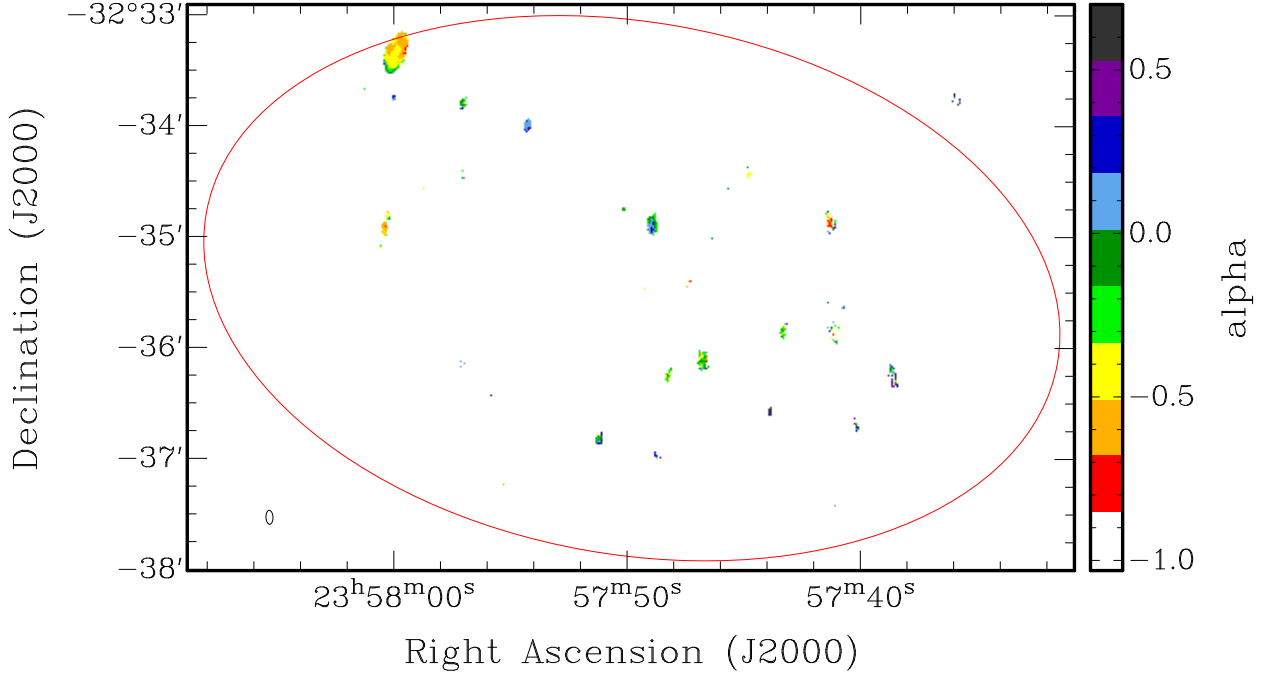


**Fig. 5** A histogram showing the distribution of flux densities of sources detected at  $\lambda = 12.2, 6$  and  $3$  cm (Table. 3; Column 5, 6 and 7). All sources have been binned in  $0.05$  mJy increments. Due to its significant flux density when compared to other discrete sources in this study, NGC7793-S26 (Table. 3; Index 61) is excluded from this graph. The dotted line represents the  $3\sigma$  level.

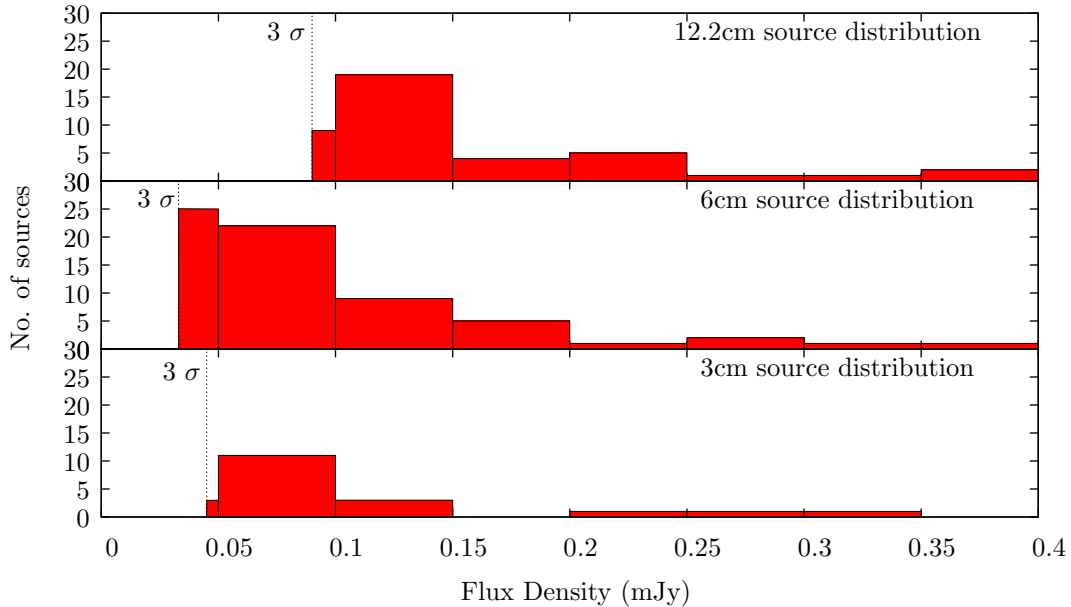
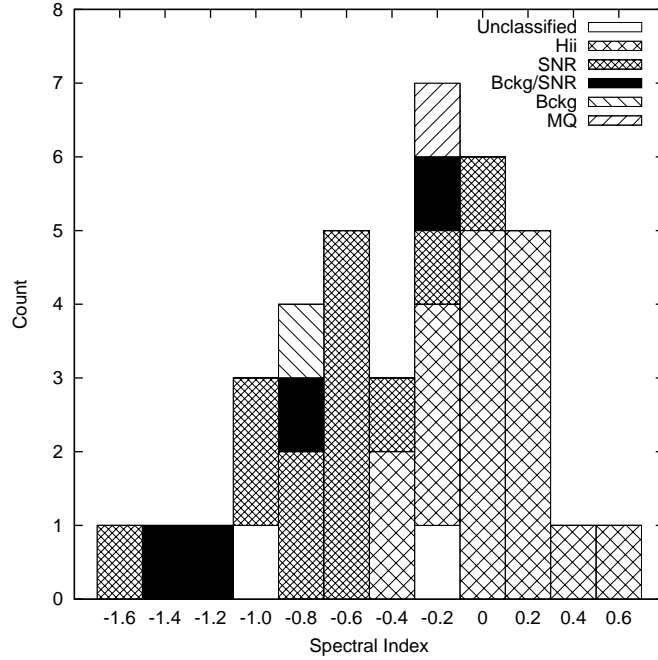


**Fig. 6** A histogram showing both the distribution of spectral indexes and classification of sources presented in Table. 3; Columns 12 and 13. J235743-323634 (Table. 3; Index. 13) is excluded from this graph.



properties it was classified as a weak candidate snr or bckg/snr. Likewise, if a source had a flat spectral index and an Infrared counterpart it was classified as a HII region candidate. If it only had one such property, it was classified as a weak HII region candidate. Each source was also visually inspected to determine if there was any intrinsic structure that would help in its identification. Three sources (Table 3; Index #26, #39 and #67) have been classified as being weak candidate snrs or bckg/snr while having a shallow spectral index. These sources were classified as either weak candidate snrs or snr/bckg based on how many counterparts were seen at additional frequency bands, the lack of extended emission or structure of the source, and the uncertainty associated with borderline steep spectral index values.

After classifying our sources we then compared them to two additional catalogues. The first catalogue, from Pannuti et al. (2002), listed a total of 33 radio and optically selected SNR candidates. A total of 5 sources were found to be common between both studies, of which we had classified 4 as SNRs and 1 which was not classified. The second catalogue, from Hodge (1969), listed HII regions. When compared to our own we find a total of 17 source matches to be common. Of these 17 sources, we had classified 12 as HII regions and 4 as SNRs. The remaining source was the micro-quasar NGC7793-S26. Hodge (1969) used two photographs, a yellow image and a yellow subtracted  $H_{\alpha}$  image, to identify HII regions. This explains why 5 sources were classified differently

when compared to Hodge (1969), as these sources would have similar optical emission. These sources are noted in Table 3.

If a source has an X-ray counterpart when compared with Pannuti et al. (2011) (Table 3; Column 11) or was listed as an SNR candidate in Pannuti et al. (2002) (as noted in Table 3; Column 14), we compared the listed positions from both catalogues. We find that the average positional difference in  $\Delta$  RA and  $\Delta$  DEC is  $-0.13''$  (with a SD of  $1.19''$ ) and  $-0.08''$  (with a SD of  $0.61''$ ) respectively.

We find 57 sources in common between radio (Figs. 1, 2 and 3) and at least one additional frequency band (Infrared, Ultra-violet, Optical and X-ray). Of these 5 frequency bands, there were 3 sources which were seen in all five, 38 in four, 11 in three and 3 in two.

### 3.3 Spectral Map

Fig. 4 shows a three point spectral map of NGC7793. Each pixel represents the spectral index as measured across Figs. 1, 2 and 3 after convolving the images to the largest beam size ( $12.2$  cm). Pixels below the 3 sigma RMS noise level for each image were ignored.

The compact sources within this study exhibit a shallow (flatish) spectral index of between  $-0.2 > \alpha > -0.4$ . This indicates dominance of regions with high thermal radiation caused by dense star formation. We can also see occasional steeper areas where  $\alpha < -0.4$ , implying a

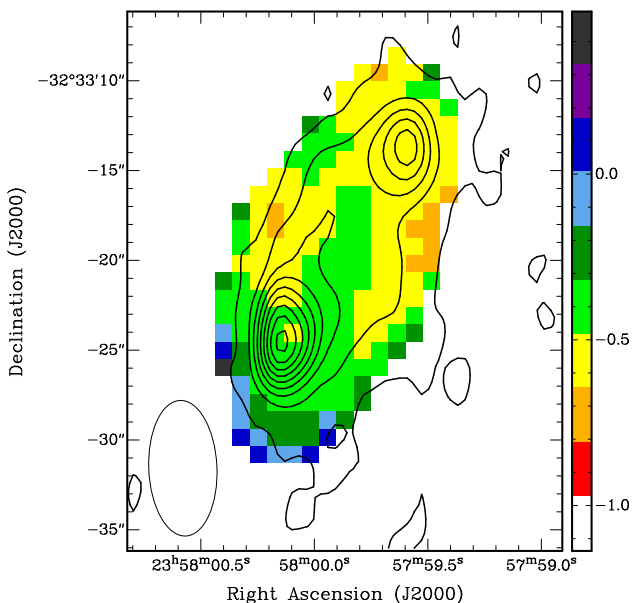
dominance of non-thermal radiation possibly caused by either synchrotron or inverse-Compton radiative mechanisms. Objects which radiate using this mechanism include SNRs and energetic jets.

### 3.3.1 Micro-quasar S26

Pakull et al. (2010) suggest that NGC 7793-S26 (Table 3; Index 61) is powered by a black hole expelling relativistic jets of matter. Through the interactions with the surrounding interstellar medium (ISM), two bubbles have formed either side of the central black hole.

Fig. 7 shows NGC7793-S26 from the spectral map (as discussed above) overlaid with contours from Fig. 2 ( $\lambda=6$  cm). When overlaid with contours, the two ISM bubbles can be clearly seen. The north most bubble (**J2000 RA=23<sup>h</sup>57<sup>m</sup>59.7<sup>s</sup>, DEC=-32°33'13.00"**) has an average spectral index of approximately  $\alpha \sim -0.54$  and range of  $-0.74$  to  $-0.24$ , while the south most bubble (**J2000 RA=23<sup>h</sup>58<sup>m</sup>00.1<sup>s</sup>, DEC=-32°33'25.00"**) has a slightly flatter average spectral index of  $\alpha \sim -0.43$  with a range of  $-0.65$  to  $-0.04$ . We also note a slightly positive index (approximately  $0 < \alpha < 0.2$ ) on the outskirts of the southern lobe.

**Fig. 7** Spectral index pixel map of NGC7793-S26 as calculated from  $\lambda=12.2, 6$  and  $3$  cm data. The image is in terms of spectral index  $\alpha$ , where  $\alpha$  is defined as  $S \propto \nu^\alpha$ . The colour bar on the right reflects the spectral index value. The synthesised beam, represented by the blue ellipse in the lower left hand corner, is  $7.56'' \times 3.80''$ . The contour levels are  $0.01$  mJy to  $0.80$  mJy with  $0.05$  mJy increments and are representative of the  $6$  cm data (Fig. 2).



The peak flux intensity of the southern lobe is measured at  $1.28$  mJy/beam,  $0.42$  mJy/beam and

$0.23$  mJy/beam at  $12.2, 6$  and  $3$  cm respectively. The northern lobe is somewhat weaker with a peak flux intensity of  $0.67$  mJy/beam at  $12.2$  cm,  $0.24$  mJy/beam at  $6$  cm and  $0.14$  mJy/beam at  $3$  cm.

## 4 Conclusion

Using archived centimetre radio-continuum observations ( $\lambda=12.2, 5.5$  and  $3$  cm) of NGC 7793 we catalogue a total of  $76$  discrete radio sources. Of these  $76$  sources, we classified a total of  $37$  sources as HII regions,  $14$  as SNRs,  $1$  as a micro-quasar,  $1$  as a background galaxy and  $4$  as either background galaxies or SNRs. A spectral index map of NGC 7793 was created which exhibited a mostly shallow spectral index value, indicating dominance of regions with high thermal radiation caused by dense star formation. We also studied the radio component of the micro-quasar NGC7793-S26, and showed that on average it has a somewhat steep spectral index of between  $-0.3$  and  $-0.7$ .

## 5 Acknowledgements

The Australia Telescope Compact Array is part of the Australia Telescope National Facility which is funded by the Commonwealth of Australia for operation as a National Facility managed by CSIRO. This paper includes archived data obtained through the Australia Telescope Online Archive (<http://atoa.atnf.csiro.au>). The Digitized Sky Surveys were produced at the Space Telescope Science Institute under U.S. Government grant NAG W-2166. The images of these surveys are based on photographic data obtained using the Oschin Schmidt Telescope on Palomar Mountain and the UK Schmidt Telescope. The plates were processed into the present compressed digital form with the permission of these institutions. This research has made use of Aladin, SIMBAD and Vizier, operated at the CDS, Strasbourg, France. We used the KARMA software package developed by the ATNF. Nicholas Seymour is the recipient of an ARC Future Fellowship. We would also like to thank the anonymous referee whose feedback greatly improved the quality of this paper.

**Table 3** List of point sources in the NGC 7793 field at  $\lambda = 12.2, 6$  and 3 cm. RA (3) and Dec (4) are in J2000 coordinates and are taken from the image with the highest resolution that a source was found in. Column 8 is the best fit spectral index for all flux measurements of a sources. **When calculating this spectral index value we assumed a error in flux density of 10% for each measurement.** Blank cells indicate no measurements were detect. The Infrared ID (8), Ultra-Violet ID (9), Optical ID (10) and X-ray ID (11) are from Kennicutt et al. (2003), Dale et al. (2009), Digital Sky Survey and Pannuti et al. (2011) respectively. † represents a point that could not be distinguished from noise as it was outside the **sensitive area of the primary beam**. Sources which are a strong candidate for their respective classification are presented in upper case, while less robust sources are presented in lower case. The notes ‘optically selected SNR’ and ‘radio selected SNR’ denotes SNR candidates and their method of identification as listed by Pannuti et al. (2002), while ‘H69’ denotes sources classified as HII by Hodge (1969).

1	2	3	4	5	6	7	8	9	10	11	12	13	14
Index	Source name	RA (J2000) (h m s)	Dec (J2000) ( $^{\circ}$ ' ")	$S_{16cm}$ (mJy)	$S_{6cm}$ (mJy)	$S_{3cm}$ (mJy)	IR ID	UV ID	Optical ID	X-ray ID	Spectral Index $\alpha$	Type	Notes
1	J235737-323547	23:57:37.0	-32:35:47.56	0.109			†						
2	J235737-323512	23:57:37.5	-32:35:12.80	0.100			†						
3	J235737-323511	23:57:37.8	-32:35:11.85	0.096			†						
4	J235738-323619	23:57:38.5	-32:36:19.31	0.120	0.120		†	Y	Y	Y	$0.00 \pm 0.25$	HII	H69
5	J235738-323611	23:57:38.6	-32:36:11.73	0.140	0.088		†	Y	Y	Y	$-0.57 \pm 0.25$	snr	H69
6	J235739-323459	23:57:39.5	-32:34:59.35	0.095			†						
7	J235741-323552	23:57:41.0	-32:35:52.80	0.244	0.270		†	Y	Y	Y	$0.13 \pm 0.25$	HII	H69
8	J235741-323451	23:57:41.3	-32:34:51.21	0.336	0.260		†	Y	Y	Y	$-0.32 \pm 0.25$	hii	H69
9	J235741-323534	23:57:41.4	-32:35:34.74	0.093	0.127		†	Y	Y	Y	$0.39 \pm 0.25$	HII	
10	J235743-323550	23:57:43.3	-32:35:50.20	0.214	0.180		†	Y	Y	Y	$-0.21 \pm 0.25$	hii	H69
11	J235743-323521	23:57:43.7	-32:35:21.70	0.160			†	Y					
12	J235743-323528	23:57:43.8	-32:35:28.47		0.047		†						
13	J235743-323634	23:57:43.8	-32:36:34.04		0.098	0.316	Y	Y	Y	Y	$2.34 \pm 0.41$		
14	J235743-323532	23:57:44.0	-32:35:32.52		0.043		†						
15	J235743-323442	23:57:44.0	-32:34:42.14	0.144			†	Y				hii	
16	J235744-323553	23:57:44.5	-32:35:53.03		0.090		†	Y	Y	Y		hii	H69
17	J235744-323425	23:57:44.8	-32:34:25.36	0.140	0.150		†	Y	Y		$0.09 \pm 0.25$	hii	
18	J235744-323531	23:57:44.8	-32:35:31.33		0.038		†	Y	Y	Y		hii	
19	J235745-323339	23:57:45.5	-32:33:39.84		0.058	0.065	Y	Y	Y		$0.23 \pm 0.41$	HII	
20	J235745-323432	23:57:45.8	-32:34:32.41		0.034		†	Y	Y			hii	
21	J235745-323524	23:57:45.9	-32:35:24.66	0.117			†			Y			
22	J235746-323533	23:57:46.2	-32:35:33.37		0.038		†	Y	Y	Y		hii	
23	J235746-323550	23:57:46.2	-32:35:50.21		0.039		†	Y	Y			hii	
24	J235746-323459	23:57:46.5	-32:34:59.56		0.034			Y		Y		hii	
25	J235746-323511	23:57:46.6	-32:35:11.15	0.104					Y				
26	J235746-323606	23:57:46.7	-32:36:06.98	0.269	0.370	0.270	Y	Y	Y	Y	$0.04 \pm 0.26$	snr	radio selected SNR
27	J235746-323336	23:57:46.7	-32:33:36.24		0.043	0.270	Y	Y	Y	Y		hii	
28	J235747-323533	23:57:47.2	-32:35:33.00		0.042		Y	Y	Y	Y		hii	
29	J235747-323523	23:57:47.3	-32:35:23.94	0.371	0.175		Y	Y	Y	Y	$-0.93 \pm 0.25$	SNR	optically selected SNR
30	J235748-323614	23:57:48.2	-32:36:14.74	0.196	0.194	0.111	Y	Y	Y	Y	$-0.40 \pm 0.30$	snr	radio selected SNR; H69
31	J235748-323654	23:57:48.3	-32:36:54.78		0.045		†						optically selected SNR
32	J235748-323658	23:57:48.8	-32:36:58.79		0.061		†	Y	Y	Y		hii	
33	J235748-323452	23:57:48.9	-32:34:52.72	0.210	0.310	0.214	Y	Y	Y	Y	$0.06 \pm 0.33$	HII	
34	J235749-323523	23:57:49.1	-32:35:23.01		0.054		Y	Y	Y	Y		hii	
35	J235749-323528	23:57:49.2	-32:35:28.23	0.126	0.065	0.053	Y	Y	Y	Y	$-0.68 \pm 0.11$	snr	
36	J235749-323525	23:57:49.7	-32:35:25.90	0.363	0.100		Y	Y	Y		$-1.59 \pm 0.25$	snr	
37	J235749-323712	23:57:49.8	-32:37:12.03		0.048		†	Y	Y			hii	
38	J235749-323723	23:57:49.9	-32:37:23.65		0.036		†						
39	J235750-323444	23:57:50.1	-32:34:44.60	0.109	0.093	0.095			Y		$-0.11 \pm 0.06$	bckg/snr	
40	J235750-323600	23:57:50.6	-32:36:00.72		0.036			Y	Y	Y		hii	
41	J235750-323417	23:57:50.8	-32:34:17.33	0.091	0.096	0.061	Y	Y	Y	Y	$-0.27 \pm 0.26$	HII	H69
42	J235751-323648	23:57:51.2	-32:36:48.03	0.140	0.160		†	Y	Y	Y	$0.17 \pm 0.25$	hii	
43	J235752-323511	23:57:52.0	-32:35:11.94	0.217	0.152	0.090	Y	Y	Y	Y	$-0.65 \pm 0.17$	snr	H69
44	J235752-323614	23:57:52.1	-32:36:14.94	0.098	0.034				Y		$-1.31 \pm 0.25$	bckg/snr	
45	J235753-323446	23:57:54.0	-32:34:46.49	0.097	0.150			Y	Y	Y	$0.54 \pm 0.25$	hii	H69
46	J235754-323359	23:57:54.2	-32:33:59.10	0.132	0.203	0.114	Y	Y	Y	Y	$-0.05 \pm 0.45$	HII	H69
47	J235754-323603	23:57:54.2	-32:36:03.97		0.038		Y	Y	Y			hii	
48	J235754-323553	23:57:54.3	-32:35:53.15		0.034		Y	Y	Y			hii	
49	J235755-323713	23:57:55.3	-32:37:13.28	0.198	0.074		†				$-1.22 \pm 0.25$	bckg/snr	
50	J235755-323408	23:57:55.4	-32:34:08.47		0.034								
51	J235755-323626	23:57:55.8	-32:36:26.96	0.110	0.122	Y					$0.21 \pm 0.41$	HII	
52	J235755-323716	23:57:56.0	-32:37:16.51		0.056		†	Y	Y	Y		hii	
53	J235756-323540	23:57:56.1	-32:35:40.42	0.105	0.073	0.055	Y	Y	Y	Y	$-0.49 \pm 0.03$	HII	
54	J235757-323607	23:57:57.0	-32:36:07.97		0.087		Y	Y	Y	Y		hii	H69
55	J235757-323347	23:57:57.0	-32:33:47.70	0.126	0.120	0.049	Y	Y	Y	Y	$-0.66 \pm 0.47$	snr	H69
56	J235757-323424	23:57:57.0	-32:34:24.11		0.044		Y	Y	Y			hii	
57	J235757-323422	23:57:57.5	-32:34:22.26		0.044								
58	J235758-323523	23:57:58.3	-32:35:23.88	0.156					Y			snr	optically selected SNR
59	J235758-323433	23:57:58.7	-32:34:33.58	0.130	0.085	0.051	Y	Y	Y	Y	$-0.70 \pm 0.13$	snr	
60	J235759-323654	23:57:59.3	-32:36:54.52		0.049	0.049	Y	Y			$0.00 \pm 0.41$	hii	
61	J235759-323317	23:58:00.0	-32:33:17.20	109.000	94.300	74.210					$-0.28 \pm 0.08$	MQ	NGC7793-S26; S26; Double source; H69
62	J235759-323343	23:58:00.0	-32:33:43.80		0.080	0.090	Y	Y	Y	Y	$0.24 \pm 0.41$	hii	H69
63	J235800-323447	23:58:00.2	-32:34:47.31	0.140	0.060		Y	Y	Y	Y	$-1.05 \pm 0.25$	snr	
64	J235800-323359	23:58:00.3	-32:33:59.79		0.060	0.055	Y	Y	Y	Y	$-0.18 \pm 0.41$	hii	
65	J235800-323455	23:58:00.4	-32:34:55.45	0.228	0.120	0.074	Y	Y	Y	Y	$-0.86 \pm 0.05$	SNR	
66	J235800-323505	23:58:00.6	-32:35:05.21	0.119	0.067	0.063	Y	Y			$-0.51 \pm 0.16$	snr	
67	J235800-323411	23:58:00.6	-32:34:11.74	0.131	0.105	Y	Y	Y	Y		$-0.27 \pm 0.25$	snr	
68	J235801-323337	23:58:01.2	-32:33:37.02	0.094	0.075		Y	Y	Y		$-0.28 \pm 0.25$		
69	J235748-323433	23:57:48.4	-32:34:33.27		0.040		Y	Y	Y			hii	
70	J235748-323439	23:57:48.9	-32:34:39.30		0.040		Y	Y	Y			hii	H69
71	J235751-323632	23:57:51.4	-32:36:32.79	0.094	0.050			Y	Y		$-0.78 \pm 0.25$	bckg/snr	
72	J235753-323643	23:57:53.6	-32:36:43.24		0.043		Y	Y	Y			hii	H69
73	J235807-323514	23:58:07.4	-32:35:14.64	0.122	0.069	0.045					$-0.76 \pm 0.04$	bckg	
74	J235804-323607	23:58:04.3	-32:36:07.19		0.049								
75	J235803-323556	23:58:03.8	-32:35:56.19		0.051								
76	J235803-323531	23:58:03.5	-32:35:31.52	0.096	0.041						$-1.05 \pm 0.25$		



## References

- W. P. Blair and K. S. Long. Identification of Supernova Remnants in the Sculptor Group Galaxies NGC 300 and NGC 7793. *Astrophys. J. Suppl. Ser.*, 108:261, January 1997. doi: 10.1086/312958.
- D. A. Dale, S. A. Cohen, L. C. Johnson, M. D. Schuster, D. Calzetti, C. W. Engelbracht, A. Gil de Paz, R. C. Kennicutt, J. C. Lee, A. Begum, M. Block, J. J. Dalcanton, J. G. Funes, K. D. Gordon, B. D. Johnson, A. R. Marble, S. Sakai, E. D. Skillman, L. van Zee, F. Walter, D. R. Weisz, B. Williams, S.-Y. Wu, and Y. Wu. The Spitzer Local Volume Legacy: Survey Description and Infrared Photometry. *Astrophys. J.*, 703:517–556, September 2009. doi: 10.1088/0004-637X/703/1/517.
- M. A. Dopita, J. L. Payne, M. D. Filipović, and T. G. Pannuti. The physical parameters of the microquasar S26 in the Sculptor Group galaxy NGC 7793. *Mon. Not. R. Astron. Soc.*, 427:956–967, December 2012. doi: 10.1111/j.1365-2966.2012.21947.x.
- T. J. Galvin, M. D. Filipović, E. J. Crawford, G. Wong, J. L. Payne, A. De Horta, G. L. White, N. Tothill, D. Drašković, T. G. Pannuti, C. K. Grimes, B. J. Cahall, W. C. Millar, and S. Laine. Radio-continuum study of the Nearby sculptor group galaxies. Part 1: NGC 300 at  $\lambda=20$  cm. *Astrophys. Space Sci.*, 340:133–142, July 2012. doi: 10.1007/s10509-012-1044-3.
- R. Gooch. Karma: Visualisation Test-Bed Toolkit, February 2011. Astrophysics Source Code Library.
- P. W. Hodge. H II Regions in Twenty Nearby Galaxies. *Astrophys. J. Suppl. Ser.*, 18:73, June 1969. doi: 10.1086/190185.
- I. D. Karachentsev, E. K. Grebel, M. E. Sharina, A. E. Dolphin, D. Geisler, P. Guhathakurta, P. W. Hodge, V. E. Karachentseva, A. Sarajedini, and P. Seitzer. Distances to nearby galaxies in Sculptor. *Astron. Astrophys.*, 404: 93–111, June 2003. doi: 10.1051/0004-6361:20030170.
- R. C. Kennicutt, G. Bendo, C. Engelbracht, K. Gordon, A. Li, G. H. Rieke, M. J. Rieke, J. D. Smith, L. Armus, G. Helou, T. H. Jarrett, H. Roussel, D. Calzetti, C. Leitherer, S. Malhotra, M. Meyer, M. W. Regan, D. A. Dale, B. Draine, A. D. Grauer, D. J. Hollenbach, L. J. Kewley, E. Murphy, M. D. Thornley, and F. Walter. SINGS: The SIRTf Nearby Galaxies Survey. In *American Astronomical Society Meeting Abstracts*, volume 35 of *Bulletin of the American Astronomical Society*, page 1351, December 2003.
- A. N. O’Brien, M. D. Filipović, E. J. Crawford, N. F. H. Tothill, J. D. Collier, A. Y. De Horta, G. F. Wong, D. Drašković, J. L. Payne, T. G. Pannuti, J. P. Napier, S. A. Griffith, W. D. Staggs, and S. Kotuš. Radio-continuum study of the nearby Sculptor group Galaxies. Part 2: NGC 55 at  $\lambda=20$ , 13, 6 and 3 cm. *Astrophys. Space Sci.*, 347:159–168, September 2013. doi: 10.1007/s10509-013-1489-z.
- M. W. Pakull and F. Grisé. Ultraluminous X-ray Sources: Beambags and Optical Counterparts. In R. M. Bandyopadhyay, S. Wachter, D. Gelino, and C. R. Gelino, editors, *A Population Explosion: The Nature & Evolution of X-ray Binaries in Diverse Environments*, volume 1010 of *American Institute of Physics Conference Series*, pages 303–307, May 2008. doi: 10.1063/1.2945062.
- M. W. Pakull, R. Soria, and C. Motch. A 300-parsec-long jet-inflated bubble around a powerful microquasar in the galaxy NGC 7793. *Nature*, 466:209–212, July 2010. doi: 10.1038/nature09168.
- T. G. Pannuti, N. Duric, C. K. Lacey, A. M. N. Ferguson, M. A. Magnor, and C. Mendelowitz. An X-Ray, Optical, and Radio Search for Supernova Remnants in the Nearby Sculptor Group Sd Galaxy NGC 7793. *Astrophys. J.*, 565: 966–981, February 2002. doi: 10.1086/337918.
- T. G. Pannuti, E. M. Schlegel, M. D. Filipović, J. L. Payne, R. Petre, I. M. Harrus, W. D. Staggs, and C. K. Lacey. A Chandra Observation of the Nearby Sculptor Group Sd Galaxy NGC 7793. *Astron. J.*, 142:20, July 2011. doi: 10.1088/0004-6256/142/1/20.
- A. M. Read and W. Pietsch. ROSAT observations of the Sculptor galaxy NGC 7793. *Astron. Astrophys.*, 341:8–22, January 1999.
- R. J. Sault and M. H. Wieringa. Multi-frequency synthesis techniques in radio interferometric imaging. *Astron. Astrophys. Suppl. Ser.*, 108:585–594, December 1994.
- R. J. Sault, P. J. Teuben, and M. C. H. Wright. MIRIAD: Multi-channel Image Reconstruction, Image Analysis, and Display, June 2011. Astrophysics Source Code Library.
- R. Soria, J. Broderick, S. Corbel, M. Pakull, and C. Motch. The newly-discovered radio/optical/X-ray microquasar in NGC 7793. *ATNF Proposal*, page 3023, April 2010.
- W. E. Wilson, R. H. Ferris, P. Axtens, A. Brown, E. Davis, G. Hampson, M. Leach, P. Roberts, S. Saunders, B. S. Koribalski, J. L. Caswell, E. Lenc, J. Stevens, M. A. Voronkov, M. H. Wieringa, K. Brooks, P. G. Edwards, R. D. Ekers, B. Emonts, L. Hindson, S. Johnston, S. T. Maddison, E. K. Mahony, S. S. Malu, M. Massardi, M. Y. Mao, D. McConnell, R. P. Norris, D. Schnitzeler, R. Subrahmanyan, J. S. Urquhart, M. A. Thompson, and R. M. Wark. The Australia Telescope Compact Array Broad-band Backend: description and first results. *Mon. Not. R. Astron. Soc.*, 416:832–856, September 2011. doi: 10.1111/j.1365-2966.2011.19054.x.